

Article

Investigation of the Ambient Temperature Influence on the PEMFC Characteristics: Modeling from a Single Cell to a Stack

Nikita Faddeev *, Evgeny Anisimov, Maxim Belichenko, Alexandra Kuriganova and Nina Smirnova

Technological Department, Platov South-Russian State Polytechnic University (NPI),
346428 Novocherkassk, Russia; chibi-totoro@yandex.ru (E.A.); maxim_belichenko@mail.ru (M.B.);
kuriganova_@mail.ru (A.K.); smirnova_nv@mail.ru (N.S.)

* Correspondence: nikita.faddeev@yandex.ru

Abstract: Power supply systems based on air-cooled proton exchange membrane fuel cell (PEMFC) stacks are becoming more popular as power sources for mobile applications. We try to create a PEMFC model that allows for predicting the PEMFC operation in various climatic conditions. A total of two models were developed and used: the membrane electrode assemble (MEA) model and the PEMFC stack model. The developed MEA model allows to determine the influence of external factors (temperature) on the PEMFC power density. The data obtained using the developed model correlate with experimental data at low ambient temperatures (10–30 °C). The difference between the simulation and experimental data is less than 10%. However, the accuracy of the model during PEMFC operation at high (>30 °C) and negative ambient temperatures remains in doubt and requires improvement. The obtained data were integrated into the air-cooled PEMFC stack model. Data of the temperature fields distribution will help to manage the processes in the PEMFC stack. The maximum temperature is slightly above 60 °C, which corresponds to the optimal conditions for the operation of the stack. The temperature gradient across the longitudinal section is very low (<20 °C), which is a positive factor for the chemical reaction. However, the temperature gradient observed across the cross section of the PEMFC stack is 30 °C. The data obtained will help to optimize the mass-dimensional characteristics of air-cooled proton exchange membrane fuel cell and increase their performance. The synergetic effect between the MEA model and the PEMFC stack model can be successfully used in the selection of materials and the development of a thermoregulation system in the PEMFC stack.

Keywords: air-cooled proton exchange membrane fuel cells; modelling; finite element method



Citation: Faddeev, N.; Anisimov, E.; Belichenko, M.; Kuriganova, A.; Smirnova, N. Investigation of the Ambient Temperature Influence on the PEMFC Characteristics: Modeling from a Single Cell to a Stack. *Processes* **2021**, *9*, 2117. <https://doi.org/10.3390/pr9122117>

Academic Editors: Giosue Giacoppo and Bruno Auvity

Received: 18 October 2021

Accepted: 22 November 2021

Published: 24 November 2021

Publisher's Note: MDPI stays neutral with regard to jurisdictional claims in published maps and institutional affiliations.



Copyright: © 2021 by the authors. Licensee MDPI, Basel, Switzerland. This article is an open access article distributed under the terms and conditions of the Creative Commons Attribution (CC BY) license (<https://creativecommons.org/licenses/by/4.0/>).

1. Introduction

Power supply systems based on air-cooled proton exchange membrane fuel cell (PEMFC) stacks are becoming more popular as power sources for mobile transport applications, robotics, and unmanned aerial vehicles (UAVs), etc. [1]. Typically, the power of such PEMFC stacks is up to a few kW [2]. The PEMFC consists of two parts: bipolar plates (BP) and membrane electrode assembly (MEA). The MEA includes only one cathode and one anode. Each of the electrodes is a catalytic layer applied to carbon paper or cloth (gas diffusion layer (GDL)). Both electrodes are in contact with a proton exchange membrane [3]. Most of the heat generated during PEMFC operation is dissipated into the surrounding atmosphere via forced air convection along the cooling channels in BP. This type of fuel cell is also termed an open cathode fuel cell because the reactant air is directly taken from and removed to the environment.

It is necessary to create a model that takes into account the influence of external factors (temperature and humidity) on the PEMFC power density to predict the PEMFC operation in different climatic conditions. Previously, research has been carried out on the operation of an air-cooled PEMFC using a climatic chamber [4]. The recorded maximum power density was below 0.2 W/cm². Another group investigated the effect of increased external temperature on the power density of a single PEMFC and a stack consisting of five

PEMFCs [5]. The PEMFCs were operated on humidified H_2 at $55\text{ }^\circ\text{C}$ at the anode, and dry, ambient air at the cathode. The observed maximum current density for the single PEMFC and stack was 0.3 A/cm^2 and 0.25 A/cm^2 , respectively. Other research has focused on modeling mass and heat transfer in air-cooled PEMFC [6–8]. Commercial ANSYS Fluent software has been used for computational fluid dynamics studies that included the foretold PEMFC performance. Akbari et al. [9] and Shahsavari et al. [10] developed a single-phase computational model of an air-cooled PEMFC using COMSOL Multiphysics[®]. The focus was put on a better understanding of the prediction of the maximum stack temperature, the thermal management, and the main temperature gradient.

The influence of external temperatures on the PEMFC start was investigated in the works of Ju H. et al. [11,12] and Tabe Y. et al. [13]. Ju H. et al. developed a multiphase transient model for investigating key transport and physical phenomena during the startup of a PEMFC from subzero temperatures. The proposed PEMFC cold-start model rigorously considers ice formation in the cathode and their complicated interactions with electrochemical reactions, mass, and heat transportation [11,12]. PEMFC cold-start characteristics was investigated experimentally. Microscopic observations were conducted to clarify the freezing mechanism; it has been shown that the freezing mechanism can be classified into two types. The first type freezes due to supercooled water at the interface between the GDL and the catalyst layer near $0\text{ }^\circ\text{C}$. The second type freezes in the cathode catalyst layer at low temperatures, such as $-20\text{ }^\circ\text{C}$ [13].

The main target of this work was the PEMFC model creation that allows for predicting the PEMFC operation in various climatic conditions. The MEA model was developed, which allow to determine the influence of external factors (temperature) on the PEMFC power density, and the obtained data were integrated into the air-cooled PEMFC stack model.

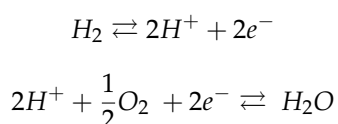
2. Materials and Methods

The PEMFC model was developed using COMSOL Multiphysics[®] (Version: 5.6.0.280) and SolidWorks Flow Simulation programs. Firstly, the MEA was modelled by the finite element method in COMSOL Multiphysics[®], the obtained data were compared with experimental data and integrated into the PEMFC stack model in SolidWorks Flow Simulation program.

2.1. MEA Simulation Model

The MEA is represented as a series of 5 adjacent homogeneous interval subdomains. This includes the 2 gas diffusion layers (GDLs) with deposited catalyst layers (CLs) and proton exchange membranes (PEM) located between them. The BPs on either end are modeled as MEA boundaries. The MEA model geometry is shown in Figure 1. The simulations were carried out for an MEA. In this case, the MEA was divided into 2,293,362 nodes and 13,224,400 elements.

The air-cooled PEMFC principle: O_2 from the air is combined with H_2 to produce electricity and H_2O . A certain amount of waste heat is produced due to overpotentials that predominantly occur at the PEMFC CLs and inside the PEM. The H_2 combustion reaction is split into two electrochemical half-reactions in PEMFCs [14]:



The reversible potential of unit fuel cell is given by the Nernst equation [15]:

$$\Delta\phi_0 = -\frac{\Delta G}{2F} + \frac{RT}{2F} \ln \left[\left(\frac{p_{H_2}}{P_{ref}} \right) \left(\frac{p_{O_2}}{P_{ref}} \right)^{1/2} \right]$$

where ΔG is change in Gibbs free energy due chemical reaction at cathode and anode, F is the Faraday constant, T is the temperature, R the gas constant, $p_{H_2} = \chi_{H_2}P$ and $p_{O_2} = \chi_{O_2}P$ are the partial pressures of hydrogen and oxygen, and $P_{ref} = 1$ atm is the reference pressure. Oxygen reduction reaction (ORR) and hydrogen oxidation reaction (HOR) in cathode and anode CLs can be described by Butler–Volmer kinetics. The rate of HOR and ORR in the CLs is thus locally given by [3]:

$$i = i_0 a \left(\exp \left[\frac{\beta 2F}{RT} \eta \right] - \exp \left[-\frac{(1-\beta)2F}{RT} \eta \right] \right)$$

with (positive) activation overpotential

$$\eta = \begin{cases} \Delta\phi - \Delta\phi_0 & \text{in anode catalyst layer (ACL)} \\ \Delta\phi_0 - \Delta\phi & \text{in cathode catalyst layer (CCL)} \end{cases}$$

$\Delta\phi = \phi_e - \phi_p$ is the Galvani potential difference between the proton and electron conducting phases (Table 1). The reversible potential difference $\Delta\phi_0$ is divided into

$$\Delta\phi_0 = \begin{cases} -\frac{T\Delta S_{HOR}}{2F} - \frac{RT}{2F} \ln \left[\frac{p_{H_2}}{P_{ref}} \right] & \text{in ACL} \\ -\frac{\Delta H - T\Delta S_{ORR}}{2F} + \frac{RT}{4F} \ln \left[\frac{p_{O_2}}{P_{ref}} \right] & \text{in CCL} \end{cases}$$

with total reaction entropy $\Delta S = \Delta S_{HOR} + \Delta S_{ORR}$. Positive i corresponds to a source of positive charge or mass in the continuity equations (Table 2).

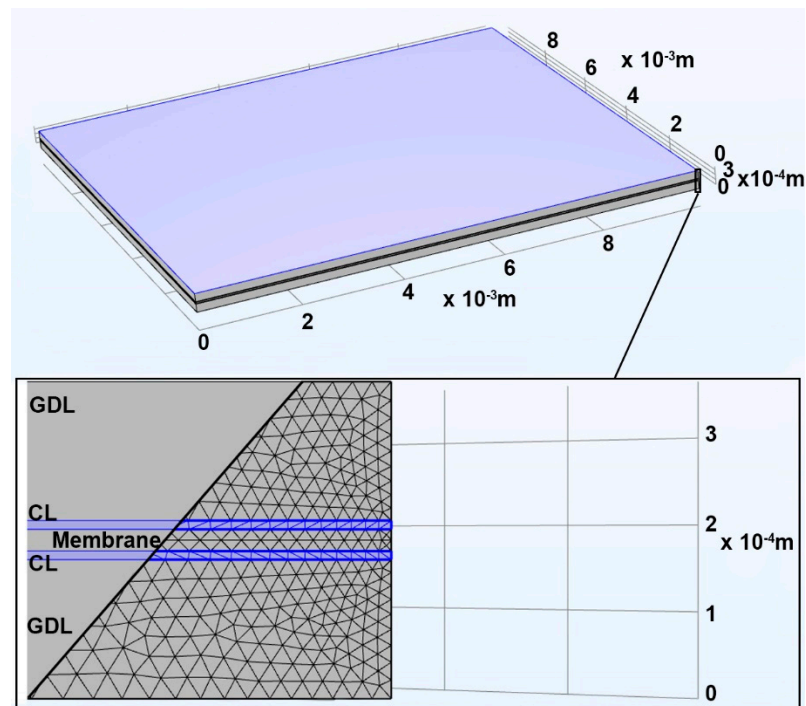


Figure 1. Geometry of the five—layer MEA model.

Transport processes of charge, energy, gas species, and water are described using coupled second-order partial differential equations (PDEs) (Table 1). Ohm's law is used to describe the flux of electrons (j_e) in the CLs and in the GDLs. The similar equation is used for the flux of protons (j_p) within the electrolyte phase of the catalyst layers and the PEM. The classical porous-electrode theory of Newman was used and adapted for this. [16]. Ohm's law governs how the flow of electrons (j_e) and protons (j_p) is controlled by a gradient of different phase potentials (ϕ_e and ϕ_p) that coexist in the catalyst layer.

Table 1. Governing equations.

Name	Flux	Continuity Equation
Ohm's law for electrons (ϕ_e)	$j_e = -\sigma_e \nabla \phi_e$	$\nabla j_e = S_e$
Ohm's law for protons (ϕ_p)	$j_p = -\sigma_p \nabla \phi_p$	$\nabla j_p = S_p$
Water transport in ionomer (λ)	$j_\lambda = -(D_\lambda/V_m) \nabla \lambda + (\xi/F) j_p$	$\nabla j_\lambda = S_\lambda$
Fourier heat conduction (T)	$j_T = -k \nabla T$	$\nabla j_T = S_T$
Darcy's law (liquid water transport) (s)	$j_s = -(\kappa/\mu V_w) (\partial p_s / \partial s) \nabla s$	$\nabla j_s = S_s$
Fickian water vapor diffusion (χ_{H_2O})	$j_{H_2O} = -CD_{H_2O} \nabla \chi_{H_2O}$	$\nabla j_{H_2O} = S_{H_2O}$
Fickian hydrogen diffusion (χ_{H_2})	$j_{H_2} = -CD_{H_2} \nabla \chi_{H_2}$	$\nabla j_{H_2} = S_{H_2}$
Fickian oxygen diffusion (χ_{O_2})	$j_{O_2} = -CD_{O_2} \nabla \chi_{O_2}$	$\nabla j_{O_2} = S_{O_2}$

Table 2. Source terms.

Source	AGDL	ACL	PEM	CCL	CGDL
S_e	0	$-i$		i	0
S_p		i	0	$-i$	
S_λ		S_{ad}	0	$S_F + S_{ad}$	
S_T	$S_{T,e}$	$S_{T,e} + S_{T,p} + S_{T,r} + S_{T,ad}$	$S_{T,p}$	$S_{T,e} + S_{T,p} + S_{T,r} + S_{T,ad} + S_{T,ec}$	$S_{T,e} + S_{T,ec}$
S_s				S_{ec}	S_{ec}
S_{H_2O}	0	$-S_{ad}$		$-S_{ad} - S_{ec}$	$-S_{ec}$
S_{H_2}	0	$-S_F$			
S_{O_2}				$-S_F/2$	0

The model by Springer et al. [17] was used for the description of water balance in the PEM. The number of H₂O molecules per acid group (λ) in the ionomer allows one to represent the degree of its humidification. The molar flux of dissolved H₂O (j_λ) is composed of the sum of its two components: electro-osmotic drag ($j_\lambda \sim j_p \sim -\nabla \phi_p$) and reverse diffusion caused by the moisture gradient ($j_\lambda \sim -\nabla \lambda$).

Fourier's law allows to describe the heat flux (j_T), which is the main method of energy transfer in the membrane-electrode assembly [18].

We used unsaturated flow theory [19] to describe the transport of liquid water. Liquid water flux is controlled by a gradient of the water saturation of pore space ∇s . This requires the specification of material properties such as the differential relationship between the saturation and capillary pressure ($\partial p_c / \partial s$) and the saturation-dependent hydraulic permeability (k).

The last 3 equations are dedicated to the gas species transport in membrane-electrode assembly. It is sufficient to consider oxygen on the cathode side, hydrogen only on the anode side, and water vapor in both gas mixtures, if gas crossover across PEM is disregarded. The simplest transport model for the gases transport is Fick's law ($j_x = -CD_x \nabla \chi_x$) [20]. The dominant transport mechanism is interred diffusion of the gas species caused by a uniform gas pressure (P) in a steady state. Thermal diffusion is disregarded. The ideal gas law is used to calculate the interstitial gas concentration $C = P/RT$.

Continuity equations for all fluxes are expressed in Table 1. Source term (S) is equating to the divergence of each flux (j).

A summary of all source term and phase transitions definitions is given in Table 2. A detailed description of the phase transitions processes associated with hydrogen oxidation, oxygen reduction and water formation in the catalyst layers is considered in one-dimensional PEMFC model taken as a basis [21].

The set of boundary conditions for this model is presented in Table 3.

The set of cell dimensions and operating conditions for this model is presented in Table 4. It shows the values of thickness, ionomer volume fraction, pore volume fraction, pore tortuosity, absolute permeability, thermal and electrical conductivity of the MEA components.

Table 3. Boundary conditions.

Variable	AGDL/AGC	ACL/AGDL	PEM/ACL	CCL/PEM	CGDL/CCL	CGC/CGDL
ϕ_e	$\phi_e = 0$	incessancy	$n j_e = 0$	$n j_e = 0$	incessancy	$\phi_e = U$
ϕ_p		$n j_p = 0$	incessancy	incessancy	$n j_p = 0$	
λ		$n j_\lambda = 0$	incessancy	incessancy	$n j_\lambda = 0$	
T	$T = T_A$	incessancy	incessancy	incessancy	incessancy	$T = T_C$
s				$n j_s = 0$	incessancy	$s = s_C$
χ_{H_2O}	$\chi_{H_2O} = \chi_{H_2O}^A$	incessancy	$n j_{H_2O} = 0$	$n j_{H_2O} = 0$	incessancy	$\chi_{H_2O} = \chi_{H_2O}^C$
χ_{H_2}	$\chi_{H_2} = \chi_{H_2}^A$	incessancy	$n j_{H_2} = 0$			
χ_{O_2}				$n j_{O_2} = 0$	incessancy	$\chi_{O_2} = \chi_{O_2}^C$

Table 4. Cell dimensions and operating conditions.

Description	Value
CL thickness	10 μm
GDL thickness	160 μm
PEM thickness	25 μm
Ionomer volume fraction in CL	0.3
Ionomer volume fraction in PEM	1
Pore volume fraction GDL	0.76
Pore volume fraction CL	0.4
Thermal conductivity GDL	1.6 W/m·K [22]
Thermal conductivity CL	0.27 W/m·K [23]
Thermal conductivity PEM	0.3 W/m·K [23]
Pore tortuosity GDL	1.6
Pore tortuosity CL	1.6
Absolute permeability GDL	$6.15 \times 10^{-12} \text{ m}^2$ [24]
Absolute permeability CL	10^{-13} m^2 [25]
Electrical conductivity GDL	1250 S/m [26]
Electrical conductivity CL	350 S/m [26]

The set of operating conditions of the base case for this model is presented in Table 5.

Table 5. Operating conditions of the base case.

Gas Pressure in Cathode and Anode	1.5 atm.
Relative Humidity in Cathode and Anode GC	100%
Liquid Saturation at GC/CGDL Interface	0.12
Ambient Temperature	−50–+50 °C
H ₂ Mole Fraction in Fuel	1.00
O ₂ Mole Fraction in Oxidant	0.21

2.2. PEM Fuel Cell Hardware Experimental Data

The catalyst inks for MEA were prepared with an ionomer (10 wt% Nafion dispersion) isopropanol and pure H₂O with the use of an ultrasonic bath for 1 h. The catalyst inks were directly sprayed onto the GDL (Freudenberg H23C3) at 80 °C to prepare the MEA. The membrane was connected to 2 GDL (Freudenberg H23C) and annealed by hot pressing at 130 °C and 80 kg/cm² for 3.5 min. PEMFC hardware (active geometric area of 4 cm²) was used to study the MEA. The Pt/C catalysts were used both at the cathode and anode CLs of MEA. The Pt loading of the cathode and anode CLs were 0.8 mg/cm² and 0.4 mg/cm², respectively. The hydrogen humidity was 100%, oxygen (air), and was used as an oxidizing agent. Gas pressure in the system: H₂—1.5 atm., air—1.5 atm. The MEA electrochemical characteristics were determined using a P-45-X potentiostat-galvanostat (Elins, Russia). The MEA was prepared in a potentiostatic mode at a voltage of 0.4 V for several hours before recording the volt-ampere curve. The study of the MEA power characteristics was carried out in a potentiostatic step mode in the voltage range of 0.9–0.2 V; the transition to

the next voltage was carried out only after the establishment of a current stationary value at a given potential.

2.3. PEMFC Stack Simulation Model

Thermo-fluid simulations of the air-cooled PEMFC stack were performed in the Solid-Works Flow Simulation program. Flow Simulation simulates the process by discretizing space and time, in such a way that the geometry of the process is divided into calculated cells, and the process time into calculated time intervals. The Navier–Stokes equation is solved for each individual computational cell. The equation is a system of partial differential equations describing the motion of a viscous Newtonian fluid. The finite element method is used to solve this system. The more elements the model is broken into, the more accurate the calculations become, but more computational resources are required to solve these equations. The grid parameters, boundary conditions, heat-generating elements, and their heat dissipation power were set for the simulation. The design of the PEMFC stack consists of the following elements:

- Air-cooled PEMFC stack;
- Number of PEMFC in stack—75 units;
- Fuel cell consists of a MEA and BP;
- Material of BP is titanium;
- BP size—40 × 240 mm;
- BP consists of 2 parts (cathode and anode);
- Anode part of the BP has smooth configuration;
- Cathode part of the BP has a channels configuration—pitch—2 mm; height—2 mm; width—2 mm;
- 2 end-plates provided at the longitudinal, opposing ends of the PEMFC stack;
- Plurality of tie rods, passing through a peripheral region of each end plate for positioning the PEMFC stack between the 2 end-plates;
- 2 fans with confuser for supplying an oxidizing agent and cooling a PEMFC stack;
- Fittings for supplying fuel (H₂), electrical leads.

The simulations were carried out for a PEMFC stack. In this case, the stack was divided into 6,818,466 cells:

- Fluid cells—3,352,729 units;
- Solid cells—3,465,737 units;
- Fluid cells contacting solids—2,500,284 units;

The simulations were carried out under the following conditions:

- Cooling and oxidizer agent –air;
- Flow rate of cooling and oxidizer agent—0.008 m³/s;
- Heat emission as a result of H₂ oxidation—50% of the nominal stack power;
- Heat transfer coefficient from PEMFC stack to outside –0*;
- Atmospheric pressure—1 atm, 101,325 Pa (in the inlet of the PEMFC stack);
- Ambient temperature—30 °C.

*—The heat transfer coefficients from PEMFC stack to outside depend on many factors (material of the PEMFC stack body, surface roughness, and whether there is additional temperature control system, etc.). It is very difficult to determine them accurately enough. Therefore, it was assumed that the heat transfer coefficients from PEMFC stack to outside is zero in this model.

3. Results and Discussion

Voltammetric and power characteristics obtained using the model and experiment are shown in Figure 2. The maximum values of the MEA power characteristics at an ambient temperature of 30 °C in the model and experiment were 0.34 W/cm² and 0.315 W/cm², respectively. Figure 2a shows that losses are associated with activation polarization in the 0.9–0.6 V region and consequently associated with the ORR kinetics. The ohmic losses

region (0.6–0.5 V) is characterized by a linear voltage—flowing current dependence due to the influence of the electrolyte and electrodes resistance to the ions and electrons transfer. At high current densities, losses associated with mass transfer dominate, which is mainly characterized by the gases supply through the porous structures of the GDLs and CLs.

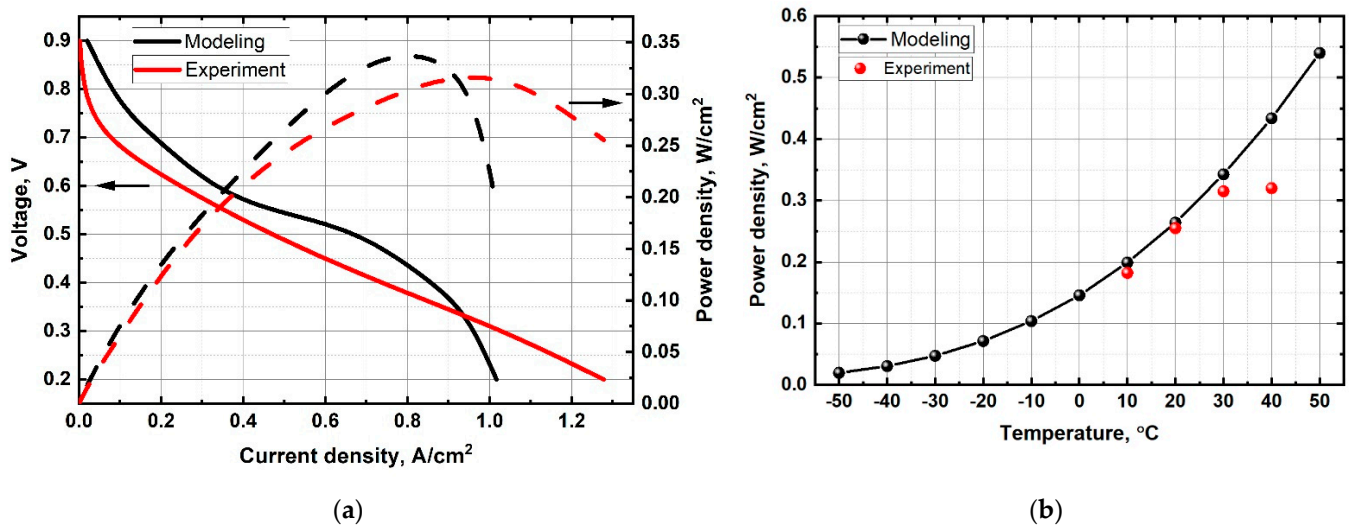


Figure 2. (a) Volt-ampere and power characteristics of MEA at an ambient temperature of 30 °C; (b) Dependence of power characteristics of MEA on ambient temperature.

The imperfection of the model leads to a difference between experimental data and model data (Figure 2b). The model does not take into account some physical and chemical processes occurring during the PEMFC operation. These processes can have a significant impact on the PEMFC power characteristics under certain operating conditions. The difference is due to the fact that the model does not account the effects of gas and heat convections, gas species permeation and pressure-driven hydraulic permeation of H₂O through the PEM, thermo-osmosis [21], non-uniformity in material properties (wettability and porosity), mechanical deformation, multi-step reaction kinetics, change of Tafel slope [27] caused by the platinum oxide formation, effects in thin, porous layers [28,29], or unsteady phenomena, etc.

The influence of electrical resistance, thermal contact resistance [30], formation and melting of ice have a particularly strong effect on the PEMFC power characteristics at high and low ambient temperatures, respectively. The difference in power characteristics between the model and experimental data becomes even greater when the ambient temperature rises above 25 °C. This is due to an increase in the resistance of current collectors when working with the fuel cell hardware and metal BPs in the PEMFC stack. The metals resistivity increases when heated (due to an increase in the speed of atoms movement in the conductor material with increasing temperature). In addition, the simulation results show the possibility of PEMFC operation at negative temperatures, because the model does not take into account the processes of ice formation and melting. The ice formation in the MEA leads to the absence of PEM proton conductivity and to the violation of its integrity under real PEMFC operating conditions. Thus, it is necessary to think over the heating system or the recuperation of the generated heat, or both, when developing the PEMFC stack, in order to solve the icing problem.

The obtained data and dependencies were used in the PEMCF stack model (power—1.5 kW) using the SolidWorks Flow Simulation program (Figure 3). Previously, we used this model to study the distribution of the oxidizer agent flows and temperature fields in dependence with location of the cooling and oxidizer supply system in the PEMFC stack [31]. The PEMFC stack consists of 75 single fuel cells (Figure 3b). The single fuel cell consists of an MEA and a bipolar plate. The bipolar plate consists of a cathode

and anode parts, that have symmetrical centers and technological holes for supplying reagents (Figure 3a). The cathode part is made as a corrugated metal plate with distribution channels of rectangular cross-sections, through which the cooling and oxidizer agent (air) is supplied. The distribution channels are as follows: configuration-pitch—2 mm, height—2 mm, width—2 mm. The anode part is flat. The connection of the cathode and anode parts is made along the bipolar plate contour at its contact points. The connection of the MEA and BP is made along the contour using a special sealant, and so this area does not participate in the electrochemical reaction. The size of a single fuel cell is 40×240 mm and has an electrochemical reaction zone of 69 cm^2 . The electrochemical reaction zone of the PEMFC stack was 5175 cm^2 . Figure 3c show image of the PEMFC stack model with the mesh.

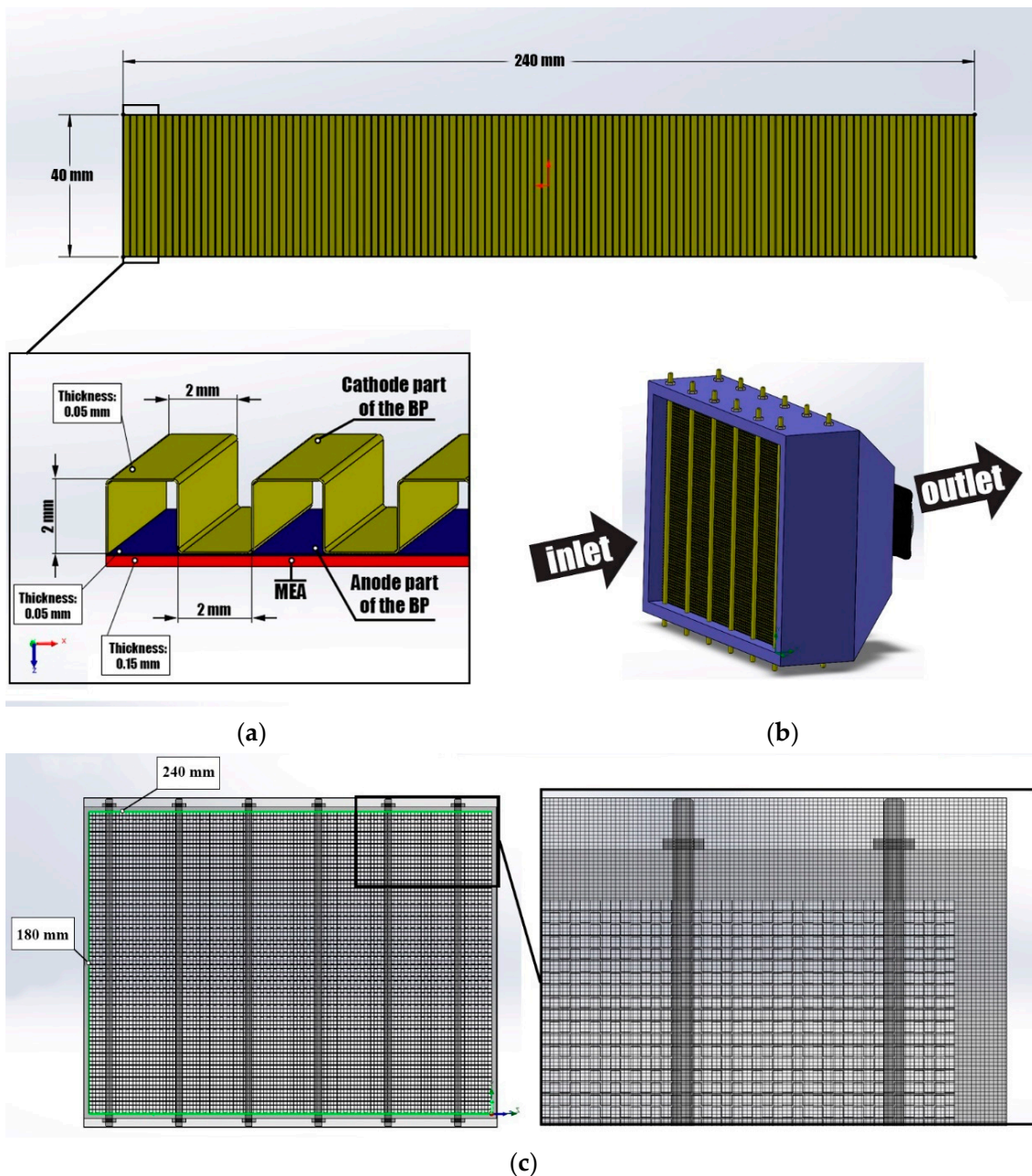


Figure 3. (a) Bipolar plate model; (b) PEMFC stack model; (c) PEMFC stack model with mesh.

The air movement and supply of clean air is carried out by mechanical means. The cooling and oxidizer supply system is made in the form of two fans installed in the PEMFC

stack body at a distance of 60 mm from the stack exit. When the cooling and oxidizer supply system is activated, air flows are evenly distributed over the entire inner surface of the PEMFC stack in BP gas distribution channels. Thus, on the front side of the PEMFC stack, the cooling and oxidizer agent is taken in and evenly distributed along the distribution channels, and air comes out from the exit from the PEMFC stack, which already takes part in the process of obtaining energy from hydrogen.

Figure 4 shows the temperature field's distribution in PEMFC stack, taking into account previously obtained data.

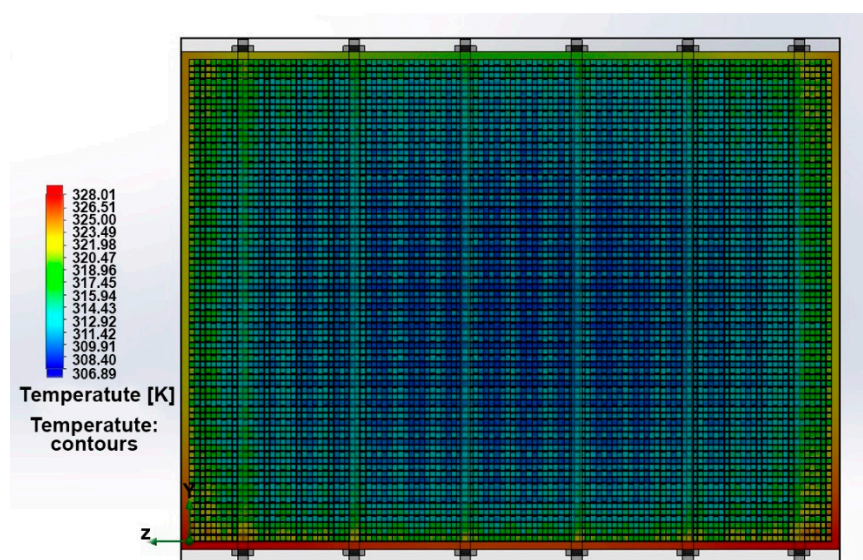


Figure 4. The distribution of temperature fields in PEMCF stack model.

A total of two fans are included in the cooling and oxidizer supply system. It may cause swirls and disturbances of the oxidizer flow due to the blades rotation that do not always have an optimal design. The PEMFC stack tie rods are opposite its exit and entry, which also may contribute swirl and disturbance to the oxidizer flow. Self-humidification happens during operation in a stack steady-state work mode. The thermophysical properties of cooling and oxidizer agent at a calculated temperature range ($0\text{ }^{\circ}\text{C}$ – $50\text{ }^{\circ}\text{C}$) are nearly independent of humidity [32]. The simulation was carried out for the most severe operating PEMFC stack conditions of zero cooling and oxidizer agent humidity.

Figure 5a,b shows the velocity field in the stack longitudinal section without and with streamlines. Streamlines make it possible to see the presence or absence of gas turbulence and stagnant zones. The movement of the oxidizer occurs uniformly along the PEMFC stack channels, and minor eddies in the area of the pins do not have a significant effect on the supply of the oxidizer to the PEMFC stack.

The temperature fields in the longitudinal and in the cross section of the stack at the inlet and outlet from the PEMFC stack are shown in Figure 6a–c. It can be seen that the stack has a maximum temperature at the outlet in the area of the fan's aerodynamic shadow. The maximum temperature is $66\text{ }^{\circ}\text{C}$, which corresponds to the optimal conditions for stack operation. The temperature gradient across the longitudinal section is very low ($<20\text{ }^{\circ}\text{C}$), which is a positive factor for chemical reaction. However, there is a large difference in the temperature gradient observed across the cross section of the PEMFC stack. The temperature difference between the inlet and outlet of the stack was $30\text{ }^{\circ}\text{C}$. The difference is caused by the fan aerodynamic shadow, but this effect can be eliminated by installing larger diameter fans. If the temperature in the cross section changes significantly, then the chemical reactions rate will also change in different parts of the fuel cell, because they are sensitive to temperature changes. Due to the uneven temperature distribution in the PEMFC stack, its output characteristics can be significantly reduced. If the PEMFC stack local temperature reaches the membrane destruction temperature ($>110\text{ }^{\circ}\text{C}$), then the

membrane may break through; and in this case, the fuel and the oxidizer may mix and, as a result, the PEMFC stack will ignite. The data also indicate that the temperature fluctuations are always present due to the unsteady nature of the flow and modeling of the air as ideal gas, resulting in convective flow and vortex genesis in the wake region behind the stack. The particle flow trajectories in the stack longitudinal section (Figure 6d) also reflect the absence of turbulence in the BP channels and in the area between the PEMFC stack and the fan.

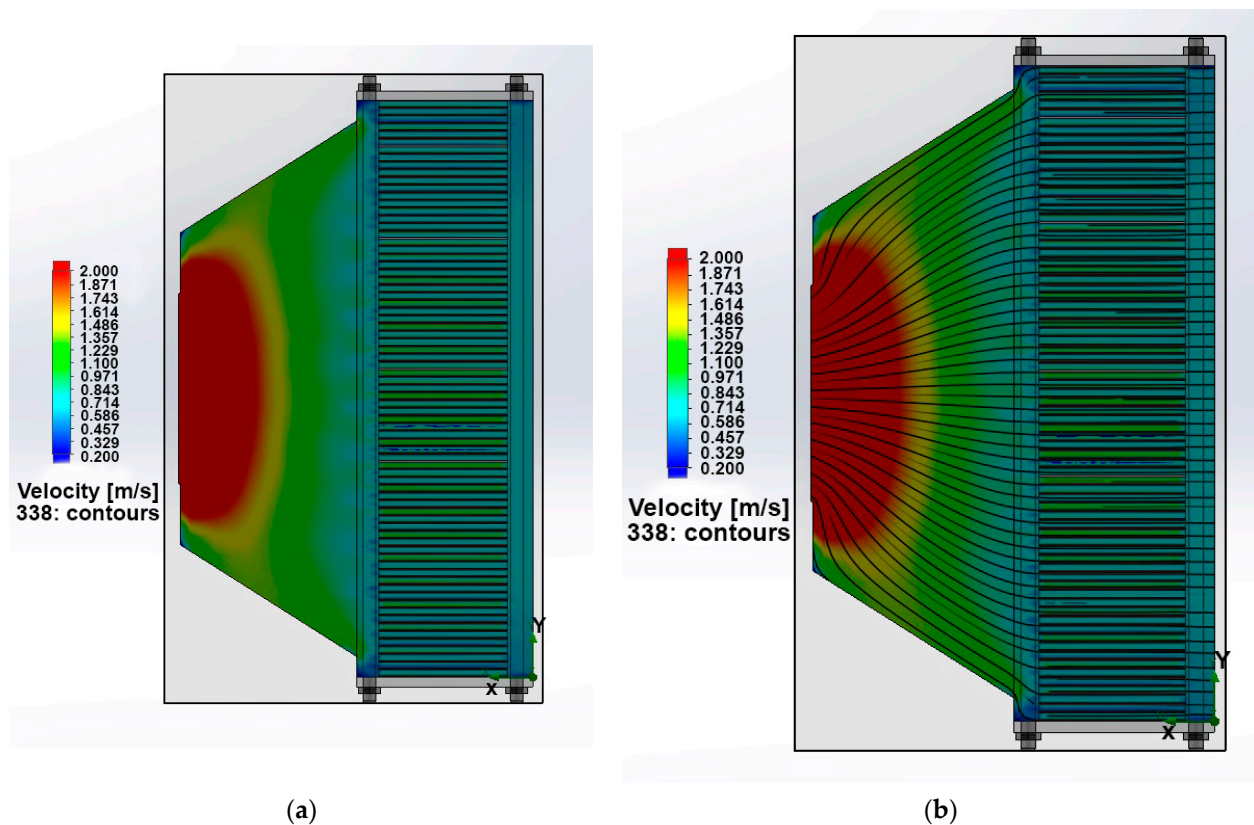


Figure 5. (a) The velocity fields of the cooling and oxidizing agent in the longitudinal section of the PEMFC stack without streamlines and (b) with streamlines.

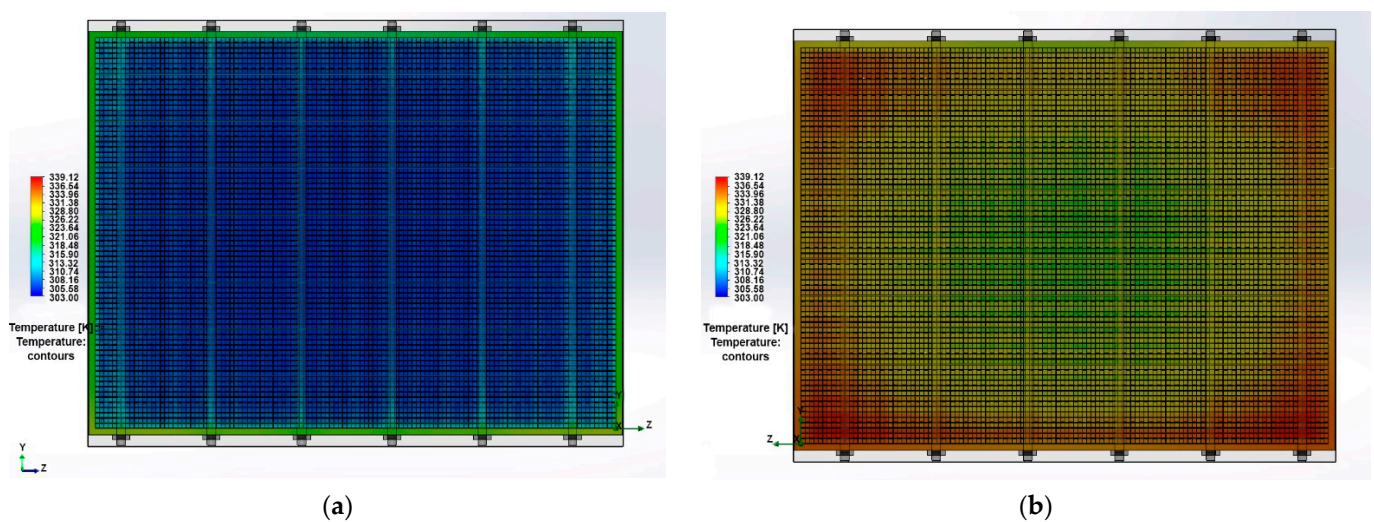


Figure 6. Cont.

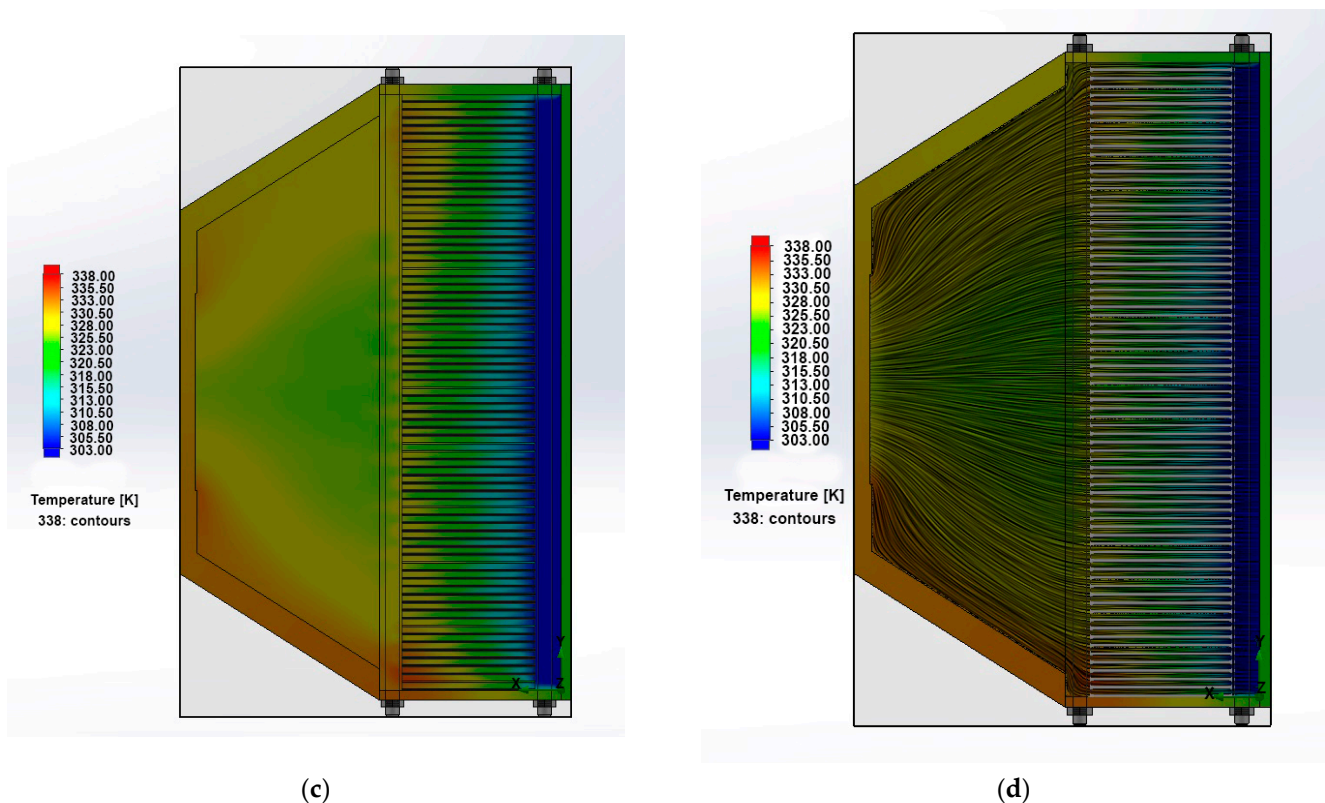


Figure 6. The temperature fields in the cross section (a) at the entry and (b) at the exit, (c) in the longitudinal section from the PEMFC stack; (d) the particle flow trajectories in the longitudinal section of the PEMFC stack.

4. Conclusions

In this paper, we try to create the PEMFC model that allows for predicting the PEMFC operation in various climatic conditions. A combined approach was applied using several simulation programs: COMSOL Multiphysics[®] to develop the MEA model and SolidWorks Flow Simulation to develop the PEMFC stack model. The developed MEA model allowed to determine the influence of external factors (temperature) on the PEMFC power density. The data obtained using the developed model correlate with experimental data at low ambient temperatures (10–30 °C). However, the accuracy of the model during PEMFC operation at high (>30 °C) and negative ambient temperatures remains in doubt and requires improvement. The obtained data were integrated into the air-cooled PEMFC stack model. The maximum temperature of the PEMFC stack is 66 °C, which corresponds to the optimal conditions for the stack operation. The temperature gradient across the longitudinal section is very low (<20 °C), which is a positive factor for the chemical reaction. However, the temperature gradient observed across the PEMFC stack cross section has a larger difference. The temperature difference between the inlet and outlet of the PEMFC stack was 30 °C. The difference is caused by the fan aerodynamic shadow, but this effect can be eliminated by installing larger diameter fans. Data of the temperature field's distribution will support the management of the processes in the air-cooled PEMFC stack. The data received will support the optimization of the mass-dimensional parameters of air-cooled PEMFC and increase its specific characteristics. The synergetic effect between the MEA model and the PEMFC stack model can be successfully used in the materials selection and for the development of a thermoregulation system in the PEMFC stack, taking into account the use in various climatic conditions. The data can be used in the design of the energy systems for mobile transport applications, robotics, and unmanned aerial vehicles, etc.

Author Contributions: Methodology, A.K.; formal analysis, M.B.; investigation, E.A.; data curation, N.F.; writing—original draft preparation, N.F.; writing—review and editing, N.F.; visualization, E.A.;

supervision, A.K.; project administration, N.S. All authors have read and agreed to the published version of the manuscript.

Funding: The article was prepared based on the results obtained during the implementation of the state assignment to carry out research on the project “Hydrogen fuel cells for small unmanned aerial vehicles: modeling, development, research” through the Ministry of Science and Higher Education of the Russian Federation (scientific code FENN-2020-0020).

Institutional Review Board Statement: Not applicable.

Informed Consent Statement: Not applicable.

Acknowledgments: This work was conducted using equipment at the Center for Shared Scientific Equipment “Nanotechnology” of the Platov South-Russian State Polytechnic University (NPI).

Conflicts of Interest: The authors declare no conflict of interest.

Nomenclature

a	Active surface area density [1/m]
a_a	Prefactor in k_a [m/s]
a_d	Prefactor in k_d [m/s]
a_{lg}	Liquid-gas interfacial area density prefactor [1/m]
r	Total interstitial gas concentration [mol/m ³]
D_X	Fickian diffusion coefficient of gas X [m ² /s]
$D_{X,ref}$	Diffusivity of X at reference conditions [m ² /s]
D_λ	Diffusion coefficient of dissolved water [m ² /s]
F	Faraday constant (96,485.333 C/mol)
f	Water volume fraction in ionomer [-]
ΔG	Gibbs free energy difference [J/mol]
ΔH	Enthalpy of formation of liquid water [J/mol]
H_{ad}	Water ab-/desorption enthalpy [J/mol]
H_{ec}	Evaporation/condensation enthalpy [J/mol]
I	Cell current density [A/m ²]
i	Electrochemical reaction rate [A/m ³]
i_0	Exchange current density [A/m ²]
j_e	Electronic flux [A/m ²]
j_p	Protonic flux [A/m ²]
j_T	Heat flux [W/m ²]
j_λ	Flux of dissolved water [mol/m ² s]
j_X	Flux of gas X [mol/m ² s]
j_s	Liquid water flux [mol/m ² s]
k	Thermal conductivity [W/mK]
k_a	Water absorption transfer coefficient [m/s]
k_c	Water condensation transfer coefficient [m/s]
k_d	Water desorption transfer coefficient [m/s]
k_e	Water evaporation transfer coefficient [m/s]
L	Layer thickness [m]
M_w	Molar mass of water [kg/mol]
n	Interfacial unit normal vector [-]
P	Absolute gas pressure [Pa]
P_A	Gas pressure in anode gas channel [Pa]
P_C	Gas pressure in cathode gas channel [Pa]
P_{ref}	Reference pressure (1 atm, 101,325 Pa)
P_{sat}	Saturation water vapor pressure [Pa]
p_c	Capillary pressure [Pa]
p_X	Partial pressure of gas X [Pa]
R	Gas constant (8.31446 J/mol K)
R_{PEM}	Membrane resistance [Ω m ²]
r	Equivalent capillary radius [m]
RH	Relative gas humidity [-]

RH_A	Relative humidity in anode gas channel [-]
RH_C	Relative humidity in cathode gas channel [-]
s	Liquid water saturation [-]
s_C	Saturation at cathode GDL/GC interface [-]
s_{im}	Immobile liquid water saturation [-]
s_{red}	Reduced liquid water saturation [-]
S_F	Substantial reaction rate [mol/m ³ s]
S_e	Electron reaction rate [A/m ³]
S_p	Proton reaction rate [A/m ³]
S_T	Heat source [W/m ³]
$S_{T,e}$	Joule heat source of electrons [W/m ³]
$S_{T,p}$	Joule heat source of protons [W/m ³]
$S_{T,r}$	Reaction heat source [W/m ³]
$S_{T,ad}$	Water ab-/desorption heat source [W/m ³]
$S_{T,ec}$	Evaporation/condensation heat source [W/m ³]
S_λ	Dissolved water reaction rate [mol/m ³ s]
S_X	Reaction rate of gas X [mol/m ³ s]
S_s	Liquid water reaction rate [mol/m ³ s]
S_{ad}	Water ab-/desorption source [mol/m ³ s]
S_{ec}	Evaporation/condensation source [mol/m ³ s]
ΔS	Reaction entropy [J/mol K]
ΔS_{HOR}	Hydrogen oxidation reaction entropy [J/mol K]
ΔS_{ORR}	Oxygen reduction reaction entropy [J/mol K]
T	Absolute temperature [K]
T_A	Temperature of anode plate and GC [K]
T_C	Temperature of cathode plate and GC [K]
T_{ref}	Reference temperature (80 °C, 353.15 K)
T	Mean MEA temperature [K]
U	Cell voltage [V]
V_m	Acid equivalent volume of membrane [m ³ /mol]
V_w	Molar volume of liquid water [m ³ /mol]
x	Through-plane coordinate [m]
x_X	Mole fraction of gas X [-]
$\chi_{H_2O}^A$	Water vapor mole fraction in anode GC [-]
$\chi_{H_2O}^C$	Water vapor mole fraction in cathode GC [-]
$\chi_{H_2}^A$	Hydrogen mole fraction in anode GC [-]
$\chi_{O_2}^C$	Oxygen mole fraction in cathode GC [-]
χ_{sat}	Saturation water vapor mole fraction [-]
α_{H_2}	Mole fraction of hydrogen in dry fuel gas [-]
α_{O_2}	Mole fraction of oxygen in dry oxidant gas [-]
β	Half-reaction symmetry factor [-]
γ	Surface tension of water [N/m]
γ_c	Water condensation rate [1/s]
γ_e	Water evaporation rate [1/s]
ε_i	Ionomer volume fraction [-]
ε_p	Pore space volume fraction (porosity) [-]
η	Activation overpotential [V]
θ	Effective contact angle [deg]
k	Hydraulic permeability [m ²]
k_{abs}	Absolute (intrinsic) permeability [m ²]
λ	Ionomer water content [-]
λ_{eq}	Equilibrium ionomer water content [-]
λ	Mean ionomer water content [-]
μ	Dynamic viscosity of liquid water [Pa s]
ζ	Electro-osmotic drag coefficient [-]
σ_e	Electric conductivity [S/m]
σ_p	Protonic conductivity [S/m]
τ	Pore tortuosity [-]
ϕ_e	Electrode phase potential [V]

ϕ_p	Electrolyte phase potential [V]
$\Delta\phi$	Galvani potential difference [V]
$\Delta\phi_0$	Reversible potential difference [V]

References

- Zhao, C.; Xing, S.; Chen, M.; Liu, W.; Wang, H. Optimal design of cathode flow channel for air-cooled PEMFC with open cathode. *Int. J. Hydrogen Energy* **2020**, *45*, 17771–17781. [\[CrossRef\]](#)
- Barbir, F. *PEM Fuel Cells: Theory and Practice*; Academic Press: Cambridge, MA, USA, 2012.
- O'Hayre, R.; Cha, S.W.; Colella, W.; Prinz, F.B. *Fuel Cell Fundamentals*; John Wiley & Sons: Hoboken, NJ, USA, 2016.
- Jeong, S.U.; Cho, E.A.; Kim, H.-J.; Lim, T.-H.; Oh, I.-H.; Kim, S.H. A study on cathode structure and water transport in air-breathing PEM fuel cells. *J. Power Sources* **2006**, *159*, 1089–1094. [\[CrossRef\]](#)
- Wu, J.; Galli, S.; Lagana, I.; Pozio, A.; Monteleone, G.; Yuan, X.Z.; Martin, J.; Wang, H. An air-cooled proton exchange membrane fuel cell with combined oxidant and coolant flow. *J. Power Sources* **2009**, *188*, 199–204. [\[CrossRef\]](#)
- Sasmito, A.P.; Birgersson, E.; Mujumdar, A.S. A novel flow reversal concept for improved thermal management in polymer electrolyte fuel cell stacks. *Int. J. Therm. Sci.* **2012**, *54*, 242–252. [\[CrossRef\]](#)
- Sasmito, A.; Lum, K.; Birgersson, E.; Mujumdar, A. Computational study of forced air-convection in open-cathode polymer electrolyte fuel cell stacks. *J. Power Sources* **2010**, *195*, 5550–5563. [\[CrossRef\]](#)
- Sasmito, A.P.; Birgersson, E.; Lum, K.; Mujumdar, A. Fan selection and stack design for open-cathode polymer electrolyte fuel cell stacks. *Renew. Energy* **2012**, *37*, 325–332. [\[CrossRef\]](#)
- Akbari, M.; Tamayol, A.; Bahrami, M. Thermal assessment of convective heat transfer in air-cooled PEMFC stacks: An experimental study. *Energy Procedia* **2012**, *29*, 1–11. [\[CrossRef\]](#)
- Shahsavari, S.; Desouza, A.; Bahrami, M.; Kjeang, E. Thermal analysis of air-cooled PEM fuel cells. *Int. J. Hydrogen Energy* **2012**, *37*, 18261–18271. [\[CrossRef\]](#)
- Ko, J.; Ju, H. Comparison of numerical simulation results and experimental data during cold-start of polymer electrolyte fuel cells. *Appl. Energy* **2012**, *94*, 364–374. [\[CrossRef\]](#)
- Chippar, P.; Ju, H. Evaluating cold-start behaviors of end and intermediate cells in a polymer electrolyte fuel cell (PEFC) stack. *Solid State Ion.* **2012**, *225*, 85–91. [\[CrossRef\]](#)
- Tabe, Y.; Saito, M.; Fukui, K.; Chikahisa, T. Cold start characteristics and freezing mechanism dependence on start-up temperature in a polymer electrolyte membrane fuel cell. *J. Power Sources* **2012**, *208*, 366–373. [\[CrossRef\]](#)
- Zhang, J. (Ed.) *PEM Fuel Cell Electrocatalysts and Catalyst Layers: Fundamentals and Applications*; Springer Science & Business Media: Berlin, Germany, 2008.
- Chavan, S.L.; Talange, D.B. Modeling and performance evaluation of PEM fuel cell by controlling its input parameters. *Energy* **2017**, *138*, 437–445. [\[CrossRef\]](#)
- Newman, J.; Tiedemann, W. Porous-electrode theory with battery applications. *AIChE J.* **1975**, *21*, 25–41. [\[CrossRef\]](#)
- Springer, T.E.; Zawodzinski, T.A.; Gottesfeld, S. Polymer electrolyte fuel cell model. *J. Electrochem. Soc.* **1991**, *138*, 2334. [\[CrossRef\]](#)
- Bhaiya, M.; Putz, A.; Secanell, M. Analysis of non-isothermal effects on polymer electrolyte fuel cell electrode assemblies. *Electrochim. Acta* **2014**, *147*, 294–309. [\[CrossRef\]](#)
- Natarajan, D.; Van Nguyen, T. A two-dimensional, two-phase, multicomponent, transient model for the cathode of a proton exchange membrane fuel cell using conventional gas distributors. *J. Electrochem. Soc.* **2001**, *148*, A1324. [\[CrossRef\]](#)
- Plawsky, J.L. *Transport Phenomena Fundamentals*; CRC Press: Boca Raton, FL, USA, 2020.
- Vetter, R.; Schumacher, J.O. Free open reference implementation of a two-phase PEM fuel cell model. *Comput. Phys. Commun.* **2019**, *234*, 223–234. [\[CrossRef\]](#)
- Burheim, O.S.; Pharoah, J.G.; Lampert, H.; Vie, P.J.S.; Kjelstrup, S. Through-plane thermal conductivity of PEMFC porous transport layers. *J. Fuel Cell Sci. Technol.* **2011**, *8*, 2. [\[CrossRef\]](#)
- Khandelwal, M.; Mench, M.M. Direct measurement of through-plane thermal conductivity and contact resistance in fuel cell materials. *J. Power Sources* **2006**, *161*, 1106–1115. [\[CrossRef\]](#)
- El-Kharouf, A.; Mason, T.J.; Brett, D.; Pollet, B.G. Ex-situ characterisation of gas diffusion layers for proton exchange membrane fuel cells. *J. Power Sources* **2012**, *218*, 393–404. [\[CrossRef\]](#)
- Yi, J.S.; Van Nguyen, T. Multicomponent transport in porous electrodes of proton exchange membrane fuel cells using the interdigitated gas distributors. *J. Electrochem. Soc.* **1999**, *146*, 38. [\[CrossRef\]](#)
- Gode, P.; Jaouen, F.; Lindbergh, G.; Lundblad, A.; Sundholm, G. Influence of the composition on the structure and electrochemical characteristics of the PEFC cathode. *Electrochim. Acta* **2003**, *48*, 4175–4187. [\[CrossRef\]](#)
- Weber, A.Z.; Borup, R.L.; Darling, R.M.; Das, P.K.; Dursch, T.J.; Gu, W.; Harvey, D.; Kusoglu, A.; Litster, S.; Mench, M.M.; et al. A critical review of modeling transport phenomena in polymer-electrolyte fuel cells. *J. Electrochem. Soc.* **2014**, *161*, F1254. [\[CrossRef\]](#)
- Holzer, L.; Pecho, O.; Schumacher, J.; Marmet, P.; Büchi, F.; Lamibrac, A.; Münch, B. Microstructure-property relationships in a gas diffusion layer (GDL) for Polymer Electrolyte Fuel Cells, Part II: Pressure-induced water injection and liquid permeability. *Electrochim. Acta* **2017**, *241*, 414–432. [\[CrossRef\]](#)

29. Holzer, L.; Pecho, O.; Schumacher, J.; Marmet, P.; Stenzel, O.; Büchi, F.; Lamibrac, A.; Münch, B. Microstructure-property relationships in a gas diffusion layer (GDL) for Polymer Electrolyte Fuel Cells, Part I: Effect of compression and anisotropy of dry GDL. *Electrochim. Acta* **2017**, *227*, 419–434. [[CrossRef](#)]
30. Vetter, R.; Schumacher, J.O. Experimental parameter uncertainty in proton exchange membrane fuel cell modeling. Part II: Sensitivity analysis and importance ranking. *J. Power Sources* **2019**, *439*, 126529. [[CrossRef](#)]
31. Anisimov, E.; Faddeev, N.; Smirnova, N. Data on the thermo-fluid simulation of open-cathode fuel cell stack depending on the location of the oxidizer/cooling supply system. *Data Brief* **2020**, *31*, 105771. [[CrossRef](#)]
32. Tsilingiris, P.T. Thermophysical and transport properties of humid air at temperature range between 0 and 100 °C. *Energy Convers. Manag.* **2008**, *49*, 1098–1110. [[CrossRef](#)]